A kinetic study of the NO to NO2 oxidation mechanism over Fe FER: a combined analysis of operando surface and gas phase data

Anna Plesniar, Irene Malpartida, Rodrigo Moraes, Olivier Marie

A kinetic study of the NO to NO_2 oxidation mechanism over Fe-FER: a combined analysis of *operando* surface and gas phase data

Olivier MARIE[a] ‡, Anna Plesniar[a], Irene Malpartida[a,b] and Rodrigo Moraes[a]

[a] *Laboratoire Catalyse et Spectrochimie, ENSICAEN, 6 Bd. Maréchal Juin, 14000, Caen, France*

[b] *now current adress: Inorganic Chemistry Department, University of Málaga & DEASYL, S.L, Spain*

Email: olivier.marie@ensicaen.fr, phone: + 33 231 452 825

‡ Corresponding author

Abstract

Diesel engines when compared with gasoline engines produce higher amount of NOx due the operating conditions. Among the NOx produced NO represents the great majority while, under air excess conditions, the removal of NOx is necessarily catalytic and still challenging. In the ammonia based SCR, it is often admitted that, when dealing with the original formulation developed for stationary sources (V/TiO_2), the fast SCR proceeds in presence of an equimolar mixture of NO and NO_2. Most of the catalytic formulations developed up to now (except Cu based zeolites) thus suffer the same rate determining step consisting in the NO to NO_2 oxidation. Aiming at improving the catalytic efficiency through the catalyst composition, it is fundamental to understand the reaction mechanism at its elementary steps in order to properly design the active sites. The choice regarding the distinct possible hypothetical mechanisms was thus here guided by the nature of the active sites. It is indeed worth knowing, for a better tuning of the catalyst formulation, whether isolated, oligomeric or dual iron sites are involved in the catalytic loop.

The approach in this work consists in a systematic study of the influence of the inlet NO concentration under O_2 excess on both the initial reaction rate (NO to NO_2 conversion level kept below 10%) and the NO coverage level onto iron measured by *operando* FTIR. Isothermal experiments were performed over an aged FeFER catalyst at three distinct temperatures. The whole set of data was then processed and compared to the expected evolution derived from five possible mechanisms. The best mechanism determined in the frame of this study involves isolated iron sites onto which NO and O_2 co-adsorb and the corresponding rate determining step consists in the dissociation of the so-formed Fe_NOO_2 intermediate species. The associated activation energy and reaction enthalpy values are then evaluated.

Key words: Mechanism, SCR, *operando*, Ferrierite, NOx, iron

1. Introduction

NOx pollution now mainly arises from road transportation: according to the European Environment Agency (EEA): this sector produces about 40.5% of the nitrogen oxides total emission [1]. The abatement of this pollutant has

been recently considered mainly in Diesel powered engines, whose operating conditions under an excess of air make the catalytic NOx reduction still challenging. Selective catalytic reduction (SCR) of NO_X compounds by ammonia (from urea) is an efficient technology for NOx removal that however lacks of activity in the low temperature range (T < 180°C) and most often also in the high temperature range (T > 500°C). The later high temperatures are however more and more encountered when an upstream Diesel Particulate Filter (DPF) is close coupled to the SCR block. In 2009 a pioneer work thus reported the possibility to develop an SCR catalyst directly dip-coated on a DPF substrate [2]. In this context, the PM oxidation occurs on the SCR layer [3] and it is thus necessary to develop a thermally durable SCR catalyst since the typical stationary source catalytic formulation (V/TiO_2) suffers from both the vaporisation of the vanadium active phase and the crystalline transition of the TiO_2 support from anatase to rutile. A quick survey of literature data reveals that alternative NH_3-SCR catalytic formulations developed for low duty vehicles are based on transition metal ion (TMI) loaded zeolites [4-6]. When considering the direct coupling of SCR onto a DPF support or resistance to ageing under high hydrothermal conditions, such zeolitic formulations [2] appear as candidate of choice with typical compositions such as Cu or Fe zeolites [7, 8]. A combined system made of Fe/SAPO-34 and Cu/CHA is even described to exhibit very good deNOX performances in a large temperature interval (200-800°C) [9].

Typically, a SCR catalyst formulation is made of acidic centres whose role consists in adsorption/activation of ammonia and red/ox centres that should provide the right NO to NO_2 ratio for fast SCR to take place when the fed flow is NO rich.

$$\text{(Fast SCR)} \qquad NO + NO_2 + 2\,NH_3 = 2\,N_2 + 3H_2O$$

When dealing with iron based zeolites, it is generally admitted that the NO to NO_2 oxidation reaction represents the RDS of the whole SCR process. This work thus aims at determining the detailed NO to NO_2 oxidation mechanism at the elemental step level on an iron loaded ferrierite (FER) preliminary aged under severe hydrothermal conditions. This investigation appears thus relevant for the evaluation of an 'underwork' DPF-SCR typical formulation and bringing insight on the mechanism at the microscopic level possibly leading to a better tuning of the active sites.

2. Material and methods

2.1 Catalyst preparation

An alkali form of ferrierite, NaK-FER, with a ratio of Si/Al = 8.8 (8 < Si/Al < 9.5), was provided by TOSOH Co., Japan (HSZ-700 series, FERRIERITE). The NH_4-FER form was prepared by up to three ion-exchange at 353 K for 3 h under vigorous stirring, with a NH_4Cl solution at a given concentration (0.10 $mol.L^{-1}$) and using the following $wt_{solution}/wt_{powder}$ = 75/1 ratio. After the exchange, the catalyst was washed with distilled water and dried at 373 K for 12 h.

The iron-containing catalyst was obtained by ion-exchange of the NH_4 form ferrierite (NH_4-FER) with a ferrous sulphate solution ($FeSO_4$) aiming at introducing the Fe^{2+} cations from the aquous solution into the zeolite pores. The ion-exchange was performed using zeolite suspension (under continuous stirring) in diluted aqueous solution $[Fe^{2+}]$ = 1.0 10^{-3} M at a kept constant pH=2. This process is fast enough to ensure within a few hours the exchanged levels required in most application of metal zeolites. The NH_4-FER zeolite (120 mg) was thus added to a continuously stirred round-bottom flask containing the $FeSO_4$ solution (V_{FeSO4}= 60 mL) in order to fix the $m_{FeSO4\ solution}/m_{zeolite}$ ratio to 500. A condensation column was connected to the flask and the solution was heated to around 80°C and stirred for 4 hours. The solution was then filtrated, under a vacuum, using a 0,45 µm filtration paper. During the filtration, distilled water was added to rinse the cake and help removing impurities dissolved in the filtrate.

Finally, the iron containing FeFER sample was submitted to an ageing procedure chosen to simulate the wet and oxidative atmosphere present at the engine exit in driving conditions with prolonged periods at rather high temperature (severe conditions). The detailed procedure of accelerated catalyst ageing under laboratory-controlled conditions is as follows. The fresh sample was loaded in a quartz reactor placed in a tubular furnace then submitted to an ageing temperature of 800°C using a 5 K/min heating rate and a 10 hours duration step. The temperature was monitored by a thermocouple in close contact with the catalyst submitted to a total gas (10% H_2O in air) volumetric flow rate of 47 cm^3_{STP}/min. The volume of catalyst was 1.4 cm^3 (bed height of 28 mm inside an 8 mm diameter cylinder) and therefore, the Gas hourly space velocity (GHSV) was around 2000 h^{-1}.

Chemical analysis of both the fresh and aged sample (now referred as FeFER800) was performed using inductively coupled plasma atom emission spectroscopy (ICP-AES) at the CNRS Centre of Chemical Analysis (Vernaison, France) and showed a constant iron loading of 0.9 wt%.

2.2 Morphology and textural analysis

The morphology of samples was studied by Scanning Electron Microscopy using a Tescan MIRA microscope. The specific surface area was determined from physical adsorption of N_2 at 77 K. The samples were first outgassed at 523 K in a dynamic vacuum for 1 h (heating rate 3 K/min). The adsorption isotherms were recorded using a Micromeritics ASAP 2020 apparatus. The low relative pressures (p/p^0) were explored using predefined tables (5.10^{-7} < P/P° < 1) with an automatic control of the N_2 added amounts. The total pore volume was determined at p/p^0 = 0.99. The monolayer volumes (approximated as the microporous volumes) were estimated using both the Brunauer-Emmett-Teller (BET) and the Langmuir models for P/P° < 0.03. Finally, the t-plot equation was applied in order to provide a further value for the monolayer volumes.

2.3 IR *operando* tests

For the *operando* experiments, a 'sandwich like' IR cell-reactor fitted with a recently designed square sample holder was used [10]. Such a modified sample holder indeed leads to a virtually perfect plug-flow reactor, which simplifies data computing, provides a better fit of the experimental data and more accurate estimates of the kinetic parameters. The experimental set-up is based on a central six ways valve allowing to submit the catalyst (shaped as a 13 mg wafer pelletized under 0.50 tons/cm^2 leading to a 40 μm thickness) to an activation procedure while simultaneously preparing and stabilizing the reaction flow. The above described catalyst shape and IR reactor cell configuration allow according to Rasmussen et al [11] to lead a kinetic study as relevant as one performed in quartz fixed bed reactor.

Before the experiments the catalysts were pretreated at 400 °C in Ar at a constant total flow rate of 20 mL min^{-1} for 1 h. The Plug Flow Reactor (PFR) cell was operated in the differential mode by restricting the NO conversion to f<10%. The inlet NO molar fraction was varied in the [100-2000 ppm] range while the O_2 molar content was kept constant at 14% (diluted in Ar). All the experiments were conduced under atmospheric pressure and three reaction temperatures were tested (100, 130 and 160°C) in the [180 000 – 240 000 h^{-1}] space velocity range. The NO and NO_x (NO + NO_2) concentrations in the outlet gas were detected with a chemiluminescence detector (Thermo Scientific Megatec Model 42i-HL).

The IR spectra relative to the catalyst under duty were collected with a Nicolet Magna 750 FT-IR spectrometer, equipped with MCT detectors. In order to ameliorate the signal/noise ratio, the number of scans accumulation was set to 64 at a spectral resolution of 4 cm^{-1}.

3. Results and Discussion

3.1 Impact of the ageing on the morphology and the texture

3.1.1 Evolution of morphology from FeFER to FeFER800

As shown on Fig. 1 (left part), the 'fresh' FeFER powder is made of 'sheet' or 'plate' like individual particles that stuck together form 'egg' like spherical agglomerates with a rather smooth external surface. A zoom on this external agglomerate surface showed that it was made of an almost perfect 'puzzle like' pavement (not shown). It was thus interesting to test whether this external surface remained as smooth as in the 'fresh' sample after ageing was conduced. The Fig. 1 right part perfectly illustrates that for the FeFER800 sample, the agglomerates external surface roughness has considerably increased.

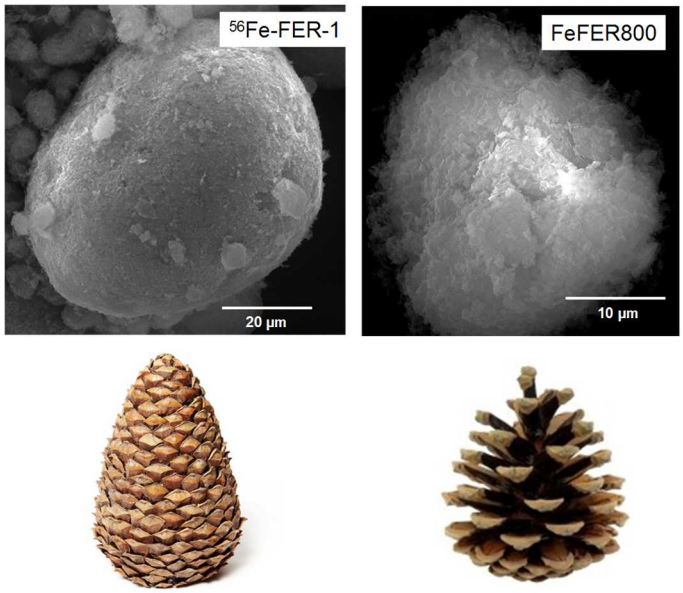

Figure 1: SEM pictures for the fresh FeFER (left) and aged FeFER800 right (upper part). Analogy with a pine cone opening to illustrate the surface roughness creation (bottom part).

For sure, it is quite difficult, (even from a few tens of pictures) to reasonably quantify the degree of roughness creation, but the analogy with a pine cone clearly reveals a general trend indicating that pine cone opening progresses upon increasing temperature up to 800°C. As a conclusion, it appears that the hydrothermal treatment favor the dislocation of agglomerates. Two hypothesis may explain this phenomenon: i) the presence of water in high temperature conditions would favor the hydrolysis of the rather soft bonds between the individual particles or/and ii) the increasing pressure inside the agglomerates upon heating would provoke the shell 'explosion'.

3.1.2 Evolution of textural properties from FeFER to FeFER800

The evaluation of the effects of the ageing procedure on the textural properties of the catalysts was carried out using the standard N_2 physisorption at liquid nitrogen temperature.

For plots relative to both FeFER and FeFER800, the isotherm was typical for the type I one (also called Langmuir isotherm) for which the adsorbed volume readily reaches a plateau ($P/P^o < 0.2$). The isotherm data were processed according to several theories (Langmuir, BET and t-plot) in order to estimate the microporous volumes. The total porous volume was directly obtained from the isotherm at $P/P^o = 0.99$ (which corresponds to the filling of pores with size below 100 nm) and then the sum of mesoporous and macroporous volumes was determined by difference. Summaries of the estimated microporous and mesoporous volumes according to the various applied isotherm processing are presented in Table 1.

Table 1. Textural characterization results for the 'fresh' FeFER and aged FeFER800 samples.

Sample	Hydrothermal and oxidative ageing 10 hours

	Microporous volume ($mL.g^{-1}$)			Mesoporous + macroporous volume ($mL.g^{-1}$)
	Langmuir	**BET**	**t-plot**	
FeFER	0.124	0.120	0.124	0.156
FeFER800	0.139	0.134	0.141	0.185

It is obvious first that for any considered sample, all the applied theories are in good agreement regarding the values obtained for the microporous volume. Furthermore, data unambiguously indicate that both the microporous and meso/macroporous volume increased upon severe hydrothermal treatment. This trend is unexpected if we consider data form the literature indicating that hydrothermal treatments provoke framework dealumination leading to the formation of extra-framework aluminium species (EFAL). Those EFAL remaining inside the microporous system should contrarily to what is observed lower the available microporous volume.

The previous data obtained form SEM indeed indicate that hydrothermal treatment favours the dislocation of agglomerates. This result explains properly the evolution of the meso/macroporous volume upon ageing but is not 'a priori' sufficient to justify the increase of the microporous system. The individual ferrierite crystals morphology has thus been considered. According to Tschernich [12], orthorhombic ferrierites are made of blades (plates or sheets) elongated along the c-axis and with commonly the {100} as the dominant plane. Taking then into account that the main 10 members ring channels run along the c-direction, it is possible to propose a model in which, for a fresh sample, a compact given agglomerate is made of a rather perfect pavement of single crystals whose staking along the c-direction is randomly imperfect, thus leading to 10 m.r. pore entrance blocking. Upon hydrothermal ageing, the agglomerate dislocation ('pine cone' opening) proceeds (see Figure 1 right part) and consequently more isolated individual crystals present a higher available microporous volume.

3.2 Preliminary tests before kinetic experiment

The determination of a reaction mechanism should not only provide information relative to the nature of active sites, the reaction intermediates but also should allow the development of a kinetic model enabling to properly describe the experimental data. However, the development of a kinetic model from a mechanism provides equations that lead to relevant and useful values only if the experiments are conduced in the chemical regime.

A set of preliminary experiments was thus achieved with the FeFER fresh sample in order to ensure that external mass transport limitations do not occur after shaping the powder in the wafer form. For this purpose, the total volumetric flow rate was varied but the contact time was kept constant by adjusting the amount of catalyst. The results are described below on **Figure 2** and obviously the reaction rate remained constant under these conditions so that external mass transport gradients may be assumed negligible [13].

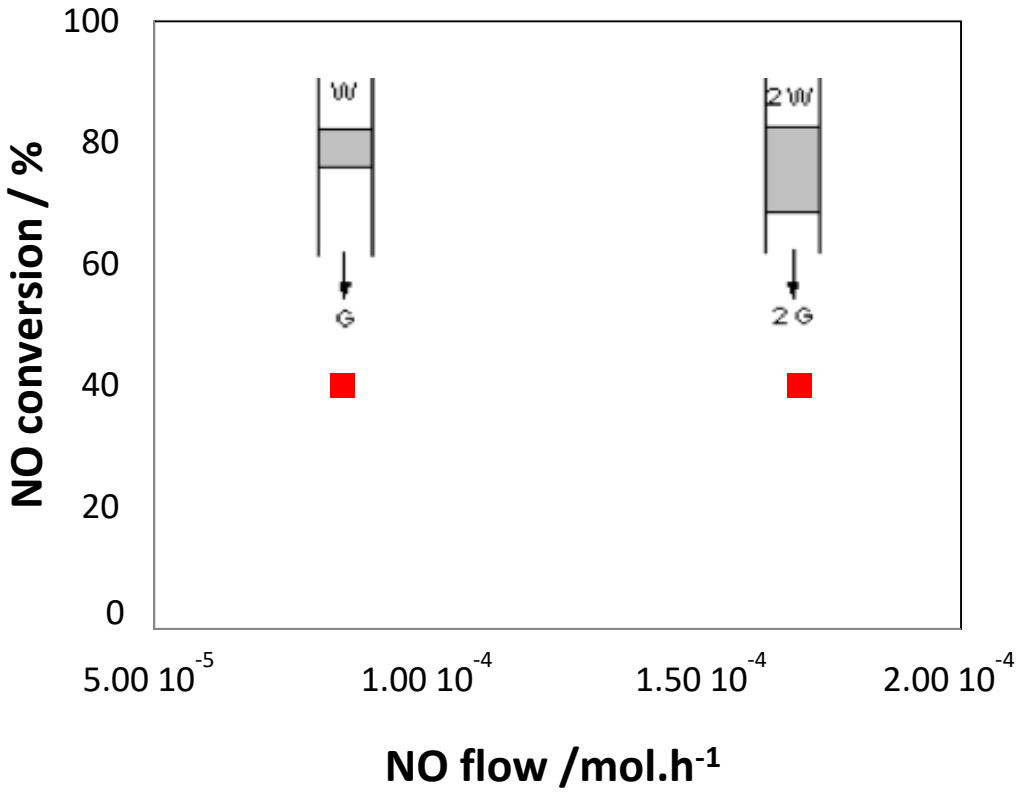

Figure 2. Verification of the absence of external diffusional limitation for the 'fresh' FeFER catalyst (W- mass of the catalyst and G- total volume NTP flow increased from 40 mL.min^{-1} to 80 mL.min^{-1})

In the regime of pore (intra-crystalline) diffusion control, the observed rate is proportional, in essence, to the ratio of the external surface to the volume of the catalyst particles. In order to evaluate the extent of internal diffusion control it is thus necessary to perform catalytic tests using zeolites with similar chemical composition but different particle size. This not an easy task and the synthesis only would require a complete dedicated study. Recent literature data were thus considered and it was found that over Cu-SSZ-13 the NH_3 oxidation reaction was in the chemical regime for reaction temperatures below 250°C [14]. Both particles size (µm range) and GHSV (200 000 – 800 000 h^{-1}) are there comparable to those reported in the present work and it was here reasonably assumed that working in the [100-160°C] range for the NO to NO_2 oxidation reaction should prevent from internal diffusion limitation.

Finally, the next part of the study will focus exclusively on the aged FeFER800 for the main reason exposed above relative to the real life of a DPF-SCR formulation. Taking into account the morphology and textural results, it then appears obvious that the 'pine cone opening' effect will further improve both the inter-particle diffusion (higher mesoporosity) and the intra-particle diffusion (higher available microporous volume) towards the iron active sites. Preliminary verifications are thus validated and further kinetic modelling arising from distinct possible mechanisms makes sense.

3.3 A combined analysis of *operando* surface and gas phase data to evaluate the NO to NO_2 oxidation mechanism

3.3.1 Catalytic data

This part will be dedicated to the description of the 'bare' catalytic data obtained from both the gas phase and the catalyst surface (*operando*) analysis over the FeFER800 catalyst.

For these experiments the mass of catalyst was w = 12.80 mg, the NO inlet molar fraction was modified while the total flow was set to 50 $NmL.min^{-1}$ (unless indicated differently). The following Table 2 reports both the inlet NO partial pressure (P_{NO}), the NO to NO_2 conversion (noted f), the specific initial reaction rate (r°) and the IR band intensity (peak height) for mononitrosyl (normalized to 1 mg of powder) where $r° = F_{NO,in} * f / w$.

$F_{NO,in}$ stands for the NO inlet molar flow.

Table 2. A compilation of catalytic data obtained for NO to NO_2 reaction over FeFER800. Total flow = 50 $mL.min^{-1}$ except for xNO labelled with ‡ where total flow = 39 $mL.min^{-1}$.

Temperature /°C	x_{NO} / ppm	P_{NO} / atm	f / %	r° / $mol.h^{-1}.g^{-1}$	[*Fe_NO] / a.u
100	178	$1.78\ 10^{-04}$	10.2	$1.75\ 10^{-04}$	$2.55\ 10^{-01}$
	257	$2.57\ 10^{-04}$	8.3	$2.04\ 10^{-04}$	$2.87\ 10^{-01}$
	434	$4.34\ 10^{-04}$	6.1	$2.54\ 10^{-04}$	$3.27\ 10^{-01}$
	601	$6.01\ 10^{-04}$	4.8	$2.77\ 10^{-04}$	$3.48\ 10^{-01}$
	888	$8.88\ 10^{-04}$	4.2	$3.58\ 10^{-04}$	$3.70\ 10^{-01}$
	1403	$1.40\ 10^{-03}$	3.6	$4.84\ 10^{-04}$	$3.67\ 10^{-01}$
130	252	$2.52\ 10^{-04}$	17.2	$4.16\ 10^{-04}$	$1.78\ 10^{-01}$
	426	$4.26\ 10^{-04}$	13.3	$5.43\ 10^{-04}$	$2.19\ 10^{-01}$
	595	$5.95\ 10^{-04}$	9.6	$5.48\ 10^{-04}$	$2.57\ 10^{-01}$
	880	$8.80\ 10^{-04}$	8.5	$7.18\ 10^{-04}$	$2.77\ 10^{-01}$
	1370	$1.37\ 10^{-03}$	6.5	$8.54\ 10^{-04}$	$3.20\ 10^{-01}$
	1537	$1.54\ 10^{-03}$	6.3	$9.29\ 10^{-04}$	$3.24\ 10^{-01}$
160	395	$3.95\ 10^{-04}$	23.0	$8.72\ 10^{-04}$	$1.36\ 10^{-01}$
	555	$5.55\ 10^{-04}$	19.6	$1.04\ 10^{-03}$	$1.66\ 10^{-01}$
	857	$8.57\ 10^{-04}$	16.2	$1.33\ 10^{-03}$	$2.09\ 10^{-01}$

	1305	1.31 10^{-03}	13.4	1.68 10^{-03}	2.40 10^{-01}
	1552 ‡	1.55 10^{-03}	15.3	1.78 10^{-03}	2.52 10^{-01}
	1823 ‡	1.82 10^{-03}	13.9	1.90 10^{-03}	2.63 10^{-01}

The Figure 3 indeed illustrates as a typical example, the evolution of the infrared spectra relative to adsorbed species detected when the NO to NO_2 reaction proceeds at 100°C over FeFER800. The change of the inlet NO concentration clearly leads to a variation of the band intensity. The most intense peak appears at 1878 cm^{-1} and is assigned to Fe^{2+} mononitrosyl species arising from the interaction of NO with iron cations located at site G of the FER structure [15, 16].

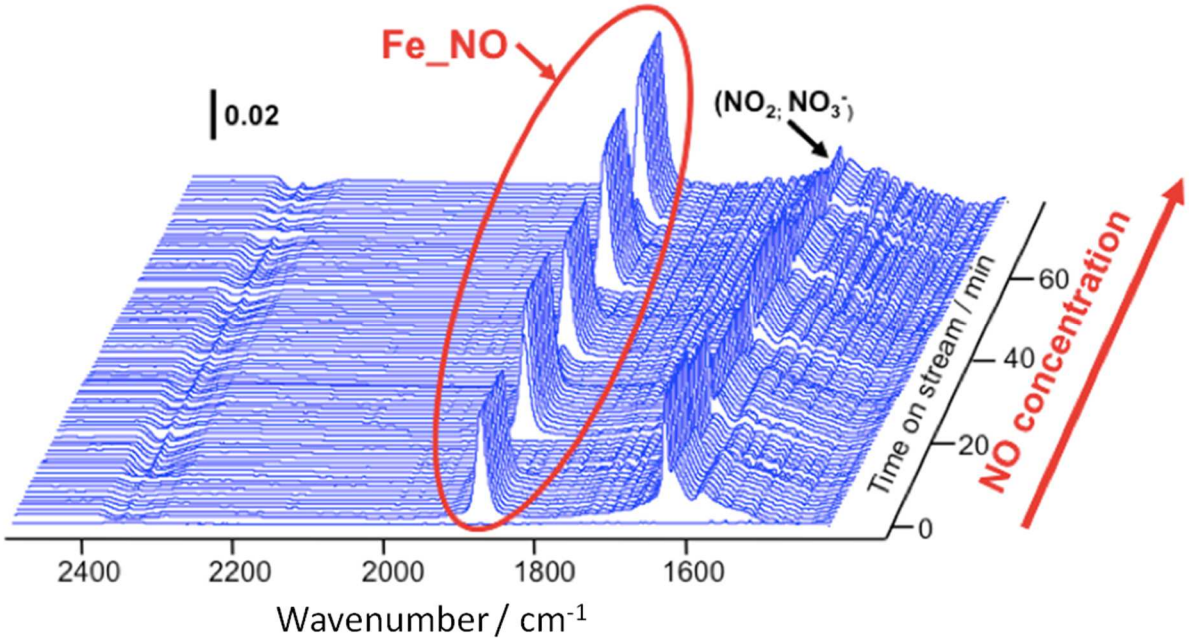

Figure 3. Iron nitrosyls intensity as a function of NO gas concentration at 100°C over FeFER800.

The region where produced NO_2 and its subsequent adsorption products are expected presents several components: two sharp ones at 1625 and 1612 cm^{-1} and a shoulder at 1575 cm^{-1}. A clear assignment to identified species tends to be complicated due to quite different data in the literature. For example, even if the presence of water traces in the flow can not totally be ruled out, the band located at 1625 cm^{-1} may also arise either from a bridging Al-nitrate species [17, 18] or from a species attached to extra-framework Fe-Al-O [19]. The 1612 cm^{-1} component can possibly be assigned to NO_2 adsorbed onto cationic species [20] but the analysis of the 1612 and 1575 cm^{-1} bands illustrates a similar evolution thus suggesting they may characterize one single species, probably an iron/aluminum based nitrate. The three later bands thus typically originate from NO_2 interaction most probably with EFAL species and it is here assumed that they do not compete for adsorption onto iron active site. As a consequence, the Table 1 only represents the evolution of the band intensity for iron mononitrosyls [*Fe_NO] here considered as the Most Abundant Reaction Intermediate species.

3.3.2 Hypothetical reaction mechanisms

In the next part of this work, five hypothetical mechanisms will be processed according to an exhaustive kinetic study. The Fig. 4 represents the various mechanisms that were tested in this study. This for sure does not represent an exhaustive list and the emphasis was put on both original hypothesis and already proposed mechanisms. The choice regarding the distinct possible hypotheses was guided by the nature of the active sites. It is indeed worth knowing, for a better tuning of the catalyst formulation, whether isolated, oligomeric or dual iron sites are involved in the catalytic loop. Different possibilities were thus investigated. The three first original hypotheses thus all require active sites close proximity. At least, dual iron sites are necessary for hypothetical mechanism 1 and 3 to take place while oligomeric species are necessary for hypothesis 2. On the contrary, hypotheses 4 and 5 involve isolated iron sites that are favoured inside the zeolite microporosity.

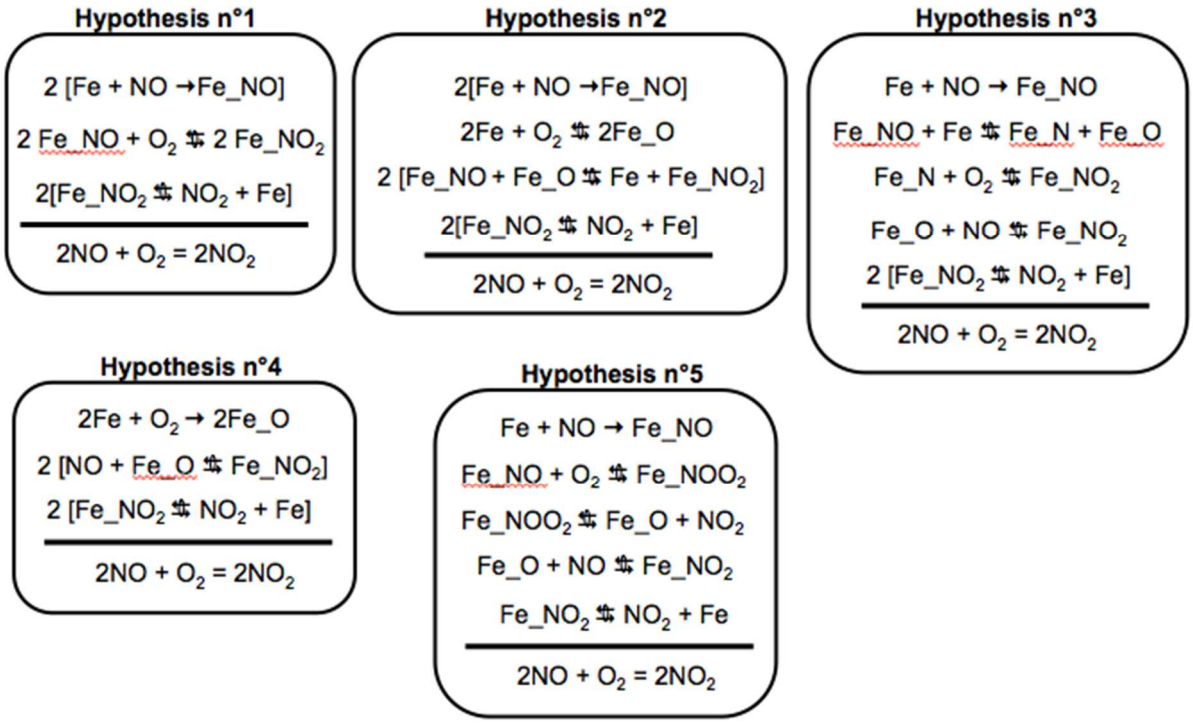

Figure 4. Five distinct hypothetical mechanisms for NO to NO_2 oxidation and their sequence of elemental steps

The first proposed hypothesis is an original and very basic one in which O_2 does not adsorb on the catalyst but directly reacts with two neighbouring adsorbed NO according to a Eley-Rideal mechanism [21]. Hypothesis 2 involving a reaction between two adsorbed species is typical for a Langmuir-Hinshelwood mechanism. Hypothesis 2 is also original and considers not only NO adsorption but also O_2 dissociative adsorption on the catalyst. Hypothesis 3, 4 and 5 involve the interaction between an adsorbed species and a gas phase molecule and could be labelled as Eley-Rideal ones. Even if more rarely met than Langmuir-Hinshelwood mechanism, the presence of isolated single sites inside zeolites onto which only one reactant may be activated in the adsorbed state

justifies the test of the Eley-Rideal mechanism. The Hypothesis 3 is original and requires the dissociative NO adsorption while mechanisms 4 and 5 come from previous works [22, 23]. The fifth hypothesis, considering the co-adsorption of NO and O_2 onto the same iron site has recently been revised from a theoretical point of view [23] while previous experimental studies had previously suggested such a mechanism [24, 25].

It seemed important, in the frame of this study, to provide all the details regarding the theoretical development of the various kinetic expressions. However, considering the whole elemental steps as possible rate determining ones for each mechanism, more than one hundred equations were obtained. As it would be fastidious to consider carefully the whole content in the core of this article, it was decided to move most of the equation development in a Supplementary Information file. In order to explain the applied methodology, the next paragraph will nevertheless detail how were obtained the rate equations for mechanism 1 in the specific case of the chemical reaction being considered as the Rate Determining Step. A summary of the possible plots and associated (hypothesis + RDS) couples will then be reported.

*3.3.3 Detailed analysis for mechanism 1: RDS considered as surface reaction from *Fe_NO*

In the context of this RDS, the other steps are considered at pseudo-equilibrium and the corresponding set of consecutive elemental steps is described below:

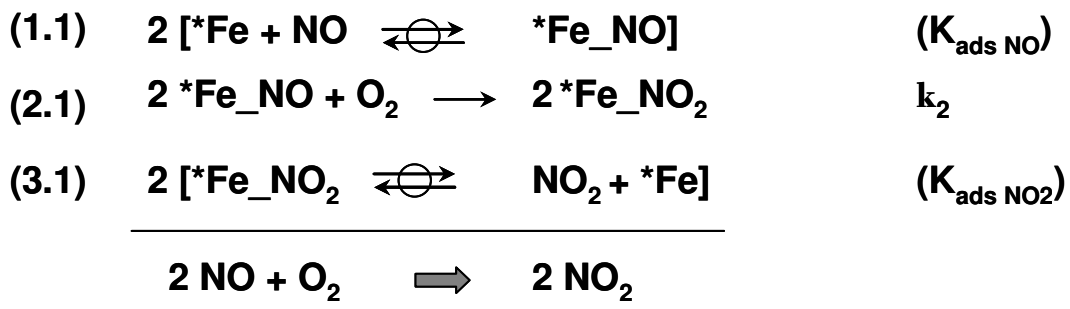

where *Fe are free superficial active sites, $K_{ads\ NO}$ is the adsorption equilibrium constants for NO, $K_{ads\ NO2}$ the adsorption equilibrium constants for NO_2 and k_2 the kinetic constant relative to step 2.1 considered here as the non reversible rate determining step (RDS). Generally speaking in the rest of this work, the step **(i.j)** notation will stand for step **i** of hypothetical mechanism **j**.

In the frame of this RDS, the reaction rate can be expressed as:

eq. 1 $$r_m = 2\,k_2[\,^*Fe\_NO]^2\,P_{O_2}$$

Consequently, the:

plot 1 $$r_m = g([\,^*Fe\_NO]^2)$$

should follow a linear evolution with E^{a}_{RDS} available via an Arrhenius plot:

The Fig. 5 upper part reports the typical plot 1 obtained at three distinct temperatures.

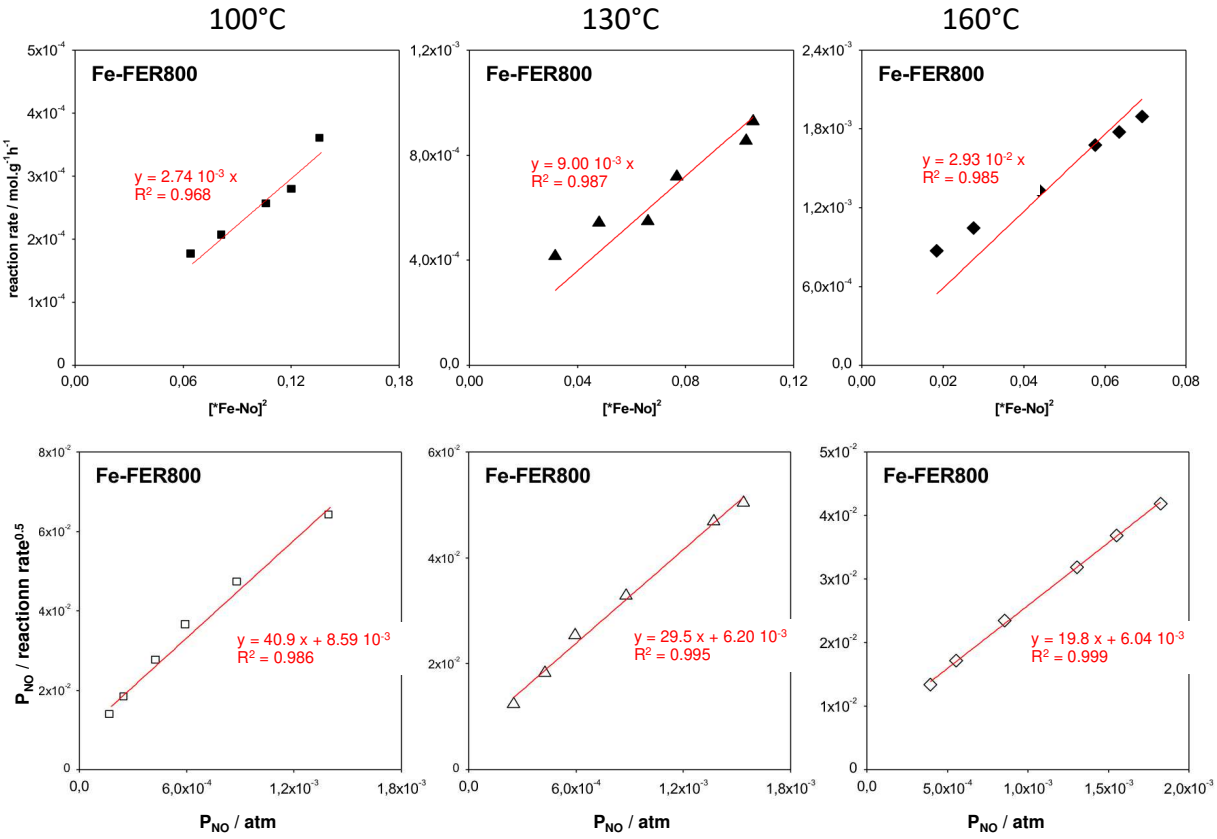

Figure 5. Kinetic processing of data obtained over FeFER800 in the frame of RDS (2.1) at distinct temperatures (Left) 100°C, middle (130°C) and right (160°C). Upper part: Plot 1 relative to *operando* adsorbed species. Lower part: Plot 2 relative to gas phase data.

Complementary, the 'classical' kinetic treatment of the 'single' gas phase data should allow to confirm/infirm the proposed RDS for the chosen mechanism. Adsorption steps 1 and 3 are quasi-equilibrated, so:

eq. 2 $$\mathbf{K_{ads\,NO}} = \frac{[\,^{*}\mathbf{Fe\_NO}]}{[\,^{*}\mathbf{Fe}]\;\;\mathbf{P_{NO}}}$$

eq. 3 $$\mathbf{K_{ads\,NO_2}} = \frac{[\,^{*}\mathbf{Fe\_NO_2}]}{[\,^{*}\mathbf{Fe}]\;\;\mathbf{P_{NO_2}}}$$

Adsorbed species similar to those previously described in the frame of this mechanism are still present under reaction conditions, and thus we still have:

eq. 4 $$\mathbf{L_{Fe}} = [\ ^{*}\mathbf{Fe}] + [\ ^{*}\mathbf{Fe\_NO}] + [\ ^{*}\mathbf{Fe\_NO_2}]$$

that gives, after introduction of eq. 2 and eq. 3:

eq. 5 $$[\ ^{*}\mathbf{Fe\_NO}\ ] = \frac{[\mathbf{L_{Fe}}]}{1 + \frac{1}{\mathbf{P_{NO}\ K_{ads\ NO}}} + \frac{\mathbf{P_{NO_2} K_{ads\ NO_2}}}{\mathbf{P_{NO}\ K_{ads\ NO}}}}$$

Taking then into account the differential conditions (conversion f < 10% in most cases and even if some values reported in Table 2 are slightly higher, they are still compatible with the assumption of differential regime), the reaction rate is finally given by the following expression (the P_{NO2} containing term in the denominator of eq. 5 has been neglected which corresponds to [*Fe_NO$_2$] << [*Fe_NO] ant traduces that iron nitrosyl are the most abundant reaction intermediate MARI):

eq. 6 $$r_m = 2\ k_2 L_{Fe}^2\ K_{ads\ NO}^2\ \frac{P_{NO}^2}{\left(1 + \mathrm{P_{NO}\ \ K_{ads\ NO}}\right)^2}\ P_{O_2}$$

Working in the differential mode of the PFR also enables to simplify $P_{NO} = P_{NO\ inlet}$ and as a constant high excess of oxygen (with respect to stoichiometry) was used, the consistency of the hypothesis could be tested since:

eq. 7 $$\sqrt{\frac{\mathbf{P_{NO\ inlet}^2}}{\mathbf{r_m}}} = \frac{\mathbf{1}}{\sqrt{\mathbf{2\ k_2 P_{O_2}}}\ \mathbf{L_{Fe}\ K_{ads\ NO}}} + \frac{\mathbf{1}}{\sqrt{\mathbf{2\ k_2 P_{O_2}}}\ \mathbf{L_{Fe}}}\ \mathbf{P_{NO\ inlet}}$$

and thus the:

plot 2 $$\sqrt{\frac{\mathbf{P_{NO\ inlet}^2}}{\mathbf{r_m}}} = \mathbf{g(P_{NO\ inlet})}$$

should be a linear one with non zero value for the y-intercept.

The Fig. 5 lower part reports the typical plot 2 obtained at three distinct temperatures. Contrarily to what is observed for plot SI 2, the experimental dispersion is here low and values for the determination coefficient R^2 are always close to unity. The (2.1 hypothesis + RDS) couple thus provides a good candidate to properly describe the catalytic behaviour. From the slope, values proportional to k_2 were obtained at a given temperature according to $2\ k_2\ P_{O_2}\ L_{Fe}^2 = \frac{1}{slope_{plot\ 2}^2}$ while the (slope $_{plot\ 2}$ / y-intercept $_{plot\ 2}$) ratio directly provides $K_{ads\ NO}$ at a given temperature. Thus, synthesizing the data obtained at several temperatures allowed to estimate both the reaction activation energy (E_{RDS}^a = 43 kJ.mol^{-1}) and the NO adsorption heat ($\Delta H_{ads\ NO}$ = -30 kJ.mol^{-1}) through Arrhenius and Van't Hoff plots respectively. These values provide useful estimations for further modelling of the whole temperature data.

3.3.4 A summary of the various possible plots after an exhaustive study of the five hypotheses

As indicated above, the full description of the detailed analysis for the four remaining hypothetical mechanisms would be fastidious here and the whole results are provided in a Supplementary Information file.

Indeed more than one hundred distinct equations were necessary to properly obtain the reaction rate equations relative to each of the elemental step as a possible RDS one for the whole hypothetical mechanisms. However, when processing the various reaction equations through linearization in order to get a first evaluation of the hypothesis validity, only six distinct plots were obtained for the *operando* (catalyst surface) data involving the intensity of adsorbed mononitrosyl species. Similarly, the reaction rate equations arising from the gas phase data lead to only five distinct plots after linearization. The table 3 provides a summary of the distinct possible plots. It is filled with the rate determining steps obtained for each given hypothesis, satisfying both the plots obtained from the *operando* data (column) and the gas phase data (raw).

Table 3. A summary of *operando* (catalyst surface) and gas phase crossed data obtained for NO to NO_2 reaction over FeFER800.

Gas phase data	Operando data: Plot SI 1	Plot 1	Plot SI 3	Plot SI 9	Plot SI 14	Plot SI 25
	$r_m = g\left(\frac{^*Fe\_NO}{f}\right)$	$r_m = g\left([\,^*Fe\_NO]^2\right)$	$r_m = g([\,^*Fe\_NO])$	$r_m = g\left(\frac{[\,^*Fe\_NO]^2}{P^2_{NO\ inlet}}\right)$	$r_m = g\left(\frac{[\,^*Fe\_NO]^2}{P_{NO\ inlet}}\right)$	$r_m = g\left(\frac{^*Fe\_NO}{f^2}\right)$
Plot SI 2: $r_m = g(P_{NO\ inlet})$	RDS 1.1 Fe+NO->FeNO RDS 1.2 Fe+NO->FeNO RDS 4.3 FeO+NO->$FeNO_2$ RDS 4.5 FeO+NO->$FeNO_2$					RDS 1.3 Fe+NO->FeNO RDS 1.5 Fe+NO->FeNO
Plot 2: $\sqrt{\frac{P^2_{NO\ inlet}}{r_m}} = g(P_{NO\ inlet})$		RDS 2.1 $2FeNO+O_2$->$2FeNO_2$				
Plot SI 4: $\frac{P_{NO\ inlet}}{r_m} = g(P_{NO\ inlet})$	RDS 5.5 $FeNO_2$->$Fe+NO_2$		RDS 3.1 $FeNO_2$->$Fe+NO_2$ RDS 4.2 $FeNO_2$->$Fe+NO_2$ RDS 5.3 $FeNO_2$->$Fe+NO_2$ RDS 2.4 FeO+NO->$FeNO_2$ RDS 3.4 $FeNO_2$->$Fe+NO_2$ RDS 2.5 $FeNO+O_2$->$FeNOO_2$ RDS 3.5 $FeNOO_2$->$FeO+NO_2$			
Plot SI 11: $\sqrt{\frac{1}{r_m}} = g(P_{NO\ inlet})$				RDS 2.2 $2Fe+O_2$->2FeO RDS 1.4 $2Fe+O_2$->2FeO		
Plot SI 16: $\sqrt{\frac{P_{NO\ inlet}}{r_m}} = g(P_{NO\ inlet})$					RDS 2.3 FeNO+Fe->FeN+FeO RDS 3.2 FeNO+FeO->$Fe+FeNO_2$	

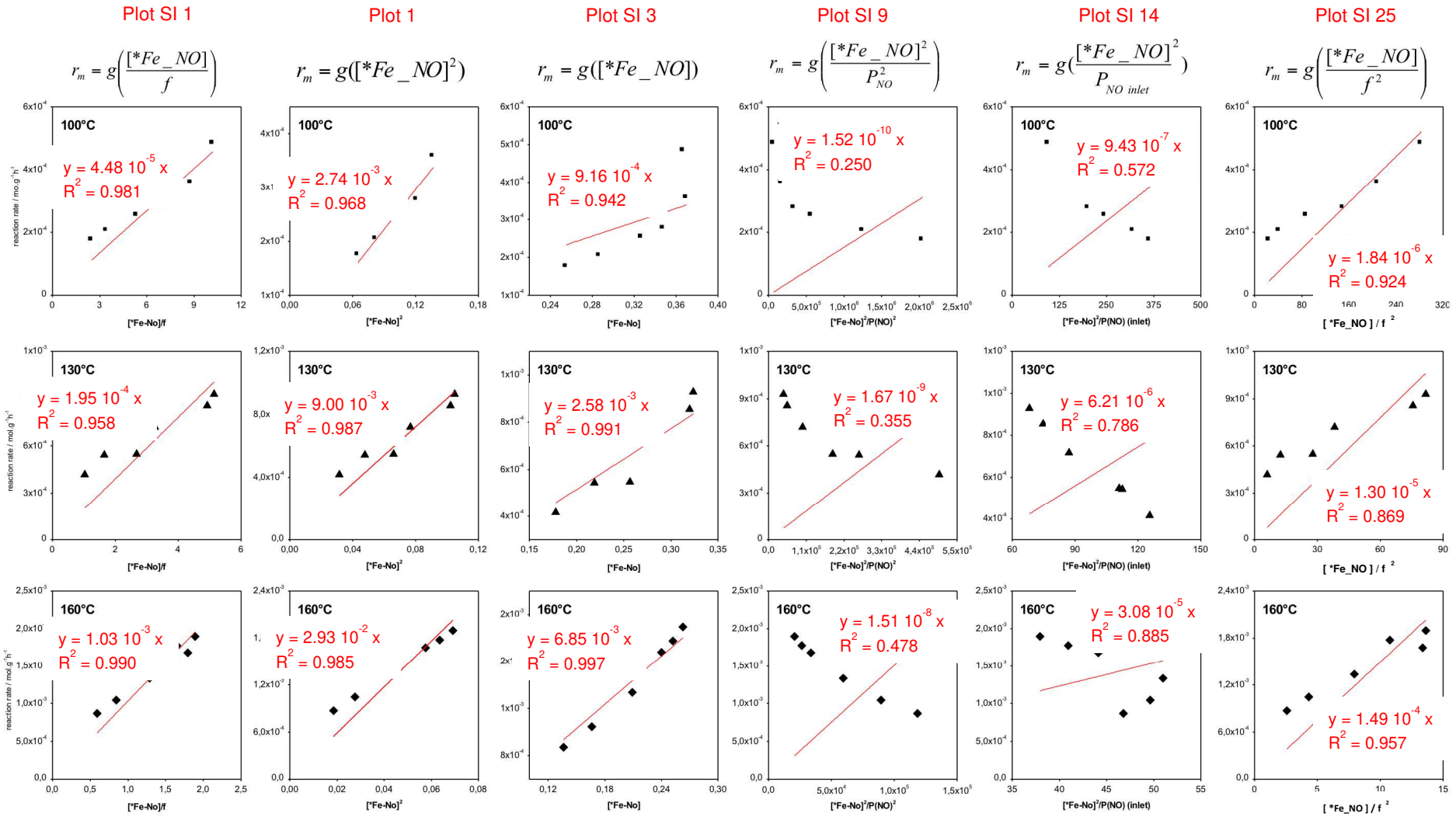

Figure 6. A summary of the possible plots arising from the kinetic processing of ***operando*** data over FeFER800; Temperature: Upper row 100°C, middle row 130°C, lower row 160°C.

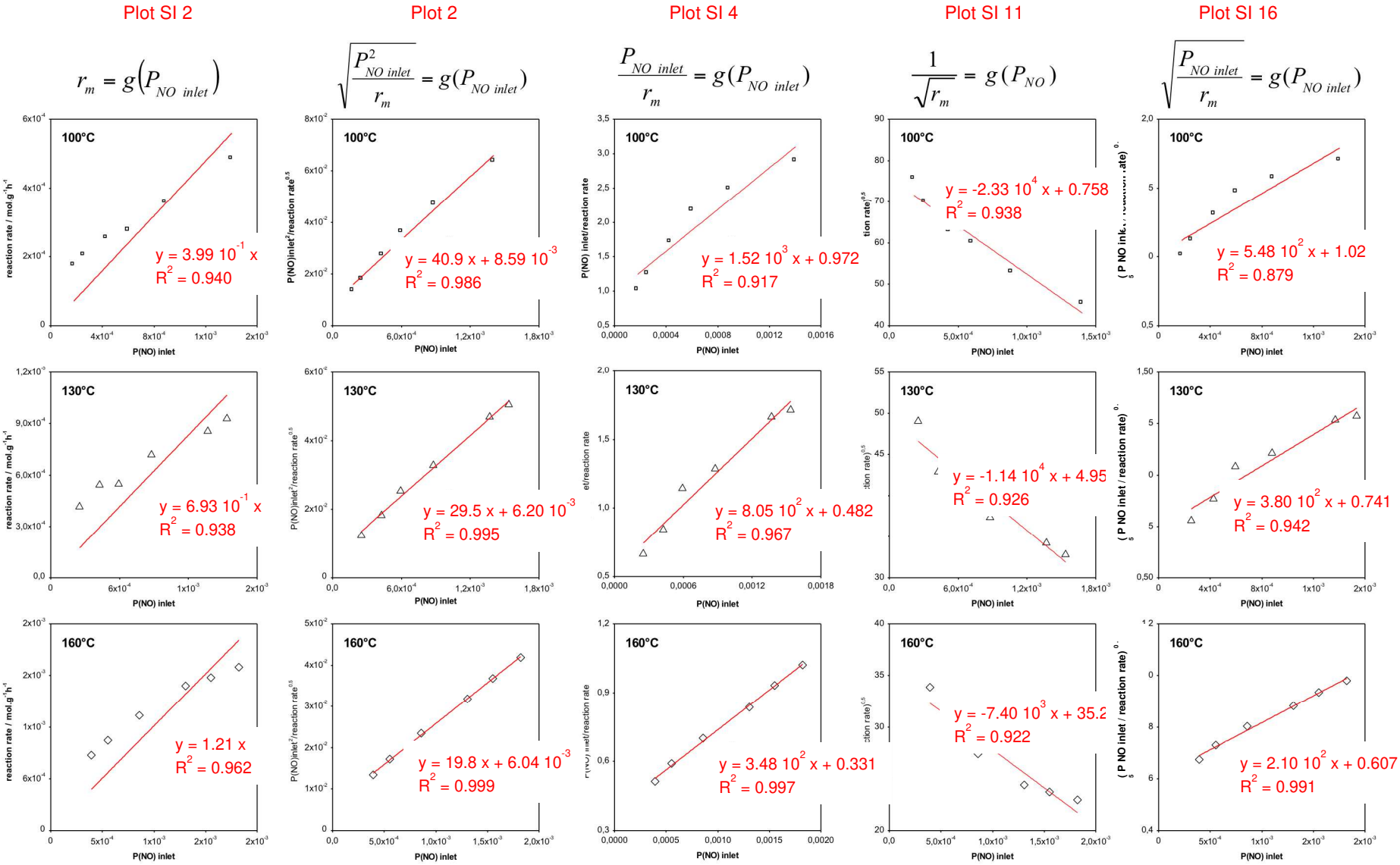

Figure 7. A summary of the possible plots arising from the kinetic processing of **gas** data over FeFER800; Temperature: Upper row 100°C, middle row 130°C, lower row 160°C

In order to provide a 'user manual' for Table 3, a simple example is given below. Assuming that step 2 of mechanism 1 is the rate determining step (RDS 2.1), the experimental data should satisfy both a linear plot 1: $r_m = g([\ ^*Fe\_NO]^2)$ and a linear plot 2: $\sqrt{\frac{\mathbf{P_{NO\ inlet}^2}}{\mathbf{r_m}}} = \mathbf{g(P_{NO\ inlet})}$. The RDS 2.1 is thus indicated in the cell at the intercept between the corresponding column and raw.

Inversely, considering the best agreement between the experimental data and the linear plots (from the determination coefficient at a first rough estimation), for both the *operando* results (see Fig. 6) and the gas phase results (see Fig. 7), it is possible to limit the amount of relevant RDS.

The detailed analysis of Fig. 6, 7 and Table 3 thus enables to clearly reject the RDS 2.2 and 1.4 as right ones since the plot SI 11: $\sqrt{\frac{\mathbf{1}}{\mathbf{r_m}}} = \mathbf{g(P_{NO\ inlet})}$ presents a negative value for its slope (whatever the reaction temperature) which is inconsistent with the theory (see pages 10 and 31 of SI file). As a consequence, plot SI 11 together with plot SI 9 whose RDS are common with those for plot SI 11 (see table 3) should be rejected.

RDS 2.3 and 3.2 should also be rejected even if the $\sqrt{\frac{\mathbf{P_{NO\ inlet}}}{\mathbf{r_m}}} = \mathbf{g(P_{NO\ inlet})}$ plot is reasonable at 160°C. Indeed, the complementary plot SI 14: $r_m = \mathrm{g}\left(\frac{[\ ^*\mathrm{Fe\_NO}\ ]^2}{\mathrm{P_{NO\ inlet}}}\right)$ arising from *operando* results presents very low determination coefficient values ($0.572 < R^2 < 0.883$) when the intercept at the origin is forced to zero. As a consequence, plot SI 14 together with plot SI 16 whose RDS are common with those for plot SI 14 (see table 3) should also be rejected.

According to the above results, the following plots SI 9, SI 11, SI 14 and SI 16 will then be disregarded and the non-relevant corresponding equations will not be considered anymore.

3.3.5 Towards the best hypothesis and its associated kinetic parameters

The preliminary fast data processing using linear regressions allowed a reduction of the number of plots to be further considered through very simple criteria: negative values of slope incompatible with the model or very low values of the determination coefficient R^2. However, when aiming at discriminating the best model, considering the R^2 value as close as possible from unity is not a reliable enough criterion. Indeed, it is worth for each possible plot to calculate a theoretical reaction rate $r_{m,theo}$ starting form values estimated through linear regression and to optimize the constant relative to the model via the minimization of the standard deviation error (SD) defined as:

$SD = \sqrt{\frac{\sum(r_{m,theo} - r_{m,exp})^2}{n-p}}$ where n represents the number of experimental points and p the number of adjustable parameters. The table 4 presents the results obtained when considering independently the *operando* and the gas phase data.

Table 4. A summary of SD values for remaining possible plots both for *operando* (catalyst surface) and gas phase data obtained for NO to NO_2 reaction over FeFER800.

		Temperature /°C	slope $_{lin}$	slope $_{opt}$	y-intercept $_{lin}$	y-intercept $_{opt}$	SD	$\sum SD$
operando data	Plot SI 1	100	$4.48\ 10^{-5}$	-	-	-	$4.70\ 10^{-5}$	$3.67\ 10^{-4}$
		130	$1.95\ 10^{-4}$	-	-	-	$1.55\ 10^{-4}$	
		160	$1.03\ 10^{-3}$	-	-	-	$1.65\ 10^{-4}$	
	Plot 1	100	$2.74\ 10^{-3}$	-	-	-	$6.11\ 10^{-5}$	$3.35\ 10^{-4}$
		130	$9.00\ 10^{-3}$	-	-	-	$8.64\ 10^{-5}$	
		160	$2.93\ 10^{-2}$	-	-	-	$1.96\ 10^{-4}$	
	Plot SI 3	100	$9.16\ 10^{-4}$	-	-	-	$8.14\ 10^{-5}$	$2.35\ 10^{-4}$
		130	$2.58\ 10^{-3}$	-	-	-	$7.08\ 10^{-5}$	
		160	$6.85\ 10^{-3}$	-	-	-	$8.31\ 10^{-5}$	
	Plot SI 25	100	$1.84\ 10^{-6}$	-	-	-	$9.35\ 10^{-5}$	$7.05\ 10^{-4}$
		130	$1.30\ 10^{-5}$	-	-	-	$2.75\ 10^{-4}$	
		160	$1.49\ 10^{-4}$	-	-	-	$3.37\ 10^{-4}$	
Gas data	Plot SI 2	100	$3.99\ 10^{-1}$	-	-	-	$8.33\ 10^{-5}$	$5.86\ 10^{-4}$
		130	$6.93\ 10^{-1}$	-	-	-	$1.88\ 10^{-4}$	
		160	1.21	-	-	-	$3.15\ 10^{-4}$	
	Plot 2	100	40.9	41.3	$8.59\ 10^{-3}$	$8.61\ 10^{-3}$	$4.43\ 10^{-5}$	$1.49\ 10^{-4}$
		130	29.5	29.6	$6.20\ 10^{-3}$	$6.19\ 10^{-3}$	$6.17\ 10^{-5}$	
		160	19.8	19.8	$6.04\ 10^{-3}$	$6.05\ 10^{-3}$	$4.31\ 10^{-5}$	
	Plot SI 4	100	$1.52\ 10^{+3}$	$1.47\ 10^{+3}$	0.972	1.03	$3.43\ 10^{-5}$	$1.09\ 10^{-4}$
		130	$8.05\ 10^{+2}$	$8.10\ 10^{+2}$	0.482	0.480	$4.97\ 10^{-5}$	
		160	$3.48\ 10^{+2}$	$3.47\ 10^{+2}$	0.331	0.333	$2.34\ 10^{-5}$	

When considering first the *operando* data, it is worth noting that for the whole plots, the rate is a linear function of a variable including the [*Fe_NO] concentration with a y-intercept fixed to zero. As a consequence, the SD values are directly provided by the Excel © LINEST function since the slope optimisation through non-linear routine is not possible. A quick comparison of the obtained SD values clearly indicates that plot SI 25 leads to the highest SD being about twice the ones calculated for the other plots. It is thus decided to reject the hypothesis leading to plot

SI 25 and the associated equations. A look at table 3 reveals that when the *operando* plot SI 25 is rejected, the *gas* plot SI 2 should also be rejected.

Indeed, when the gas data shown at table 4 are considered, the highest SD value obtained for plot SI 2 (about 4 times the one obtained for other plots) confirms that it should not be considered anymore. Concerning plot 2 and plot SI 4, non-linear optimization of slope $_{lin}$ and y-intercept $_{lin}$ through minimization of the SD values were performed using the Excel © SOLVER tool. New values for slope $_{opt}$ and y-intercept $_{opt}$ were then obtained and the comparison of the minimized SD values indicates that plot SI 4 appears to be slightly better than plot 2 contrarily to what would have been concluded from simple comparison of R^2 values (see Fig. 7).

At this step of the study, only remain as possible plots, 1, SI 1 and SI 3 for the *operando* data and 2 and SI 4 for the gas phase data. However, a focus on the grey zone of table 3 reveals that nine among nineteen distinct RDS (i.j) still remain as good candidates. Aiming at identifying the best one, the next step will thus consist for each remaining possible RDS (i.j) in processing simultaneously both the whole data (*operando* + gas) and the whole temperatures. Indeed, when a given reaction mechanism and its identified RDS are relevant, the theoretical fit of the experimental data should be valid whatever the temperature according to Arrhenius/Van't Hoff law. The example for RDS (2.1) will be detailed below while a summary table will then be provided for brevity seek.

3.3.5.1. RDS (2.1) whole data processing.

The equations relative to step 2 considered as the RDS for hypothetical mechanism 1 were exhaustively described in the core of the paper. Concerning the rate as a function of [*Fe_NO], the eq. 1 was obtained while eq. 6 describes the rate as a function of gas phase data only (see section 3.3.3)

eq. 1 $$\boldsymbol{r_m = 2\, k_2 [\,{}^{*}Fe\_NO]^2\, P_{O_2}}$$

eq. 6 $$r_m = 2\, k_2 L_{Fe}^2\, K_{ads\,NO}^2\, \frac{P_{NO}^2}{\left(1+ \mathrm{P_{NO}}\ \ \mathrm{K_{ads\,NO}}\right)^2}\, P_{O_2}$$

Aiming at considering the whole temperatures simultaneously, eq. 1 and eq. 6 convert into eq. 8 and eq. 9 respectively.

eq. 8 $$r_m = 2\, A_2\, e^{\left(\frac{-E_{RDS}^a}{RT}\right)} P_{O_2}\, [*\,Fe\_NO]^{\,2}$$

eq. 9 $$r_m = \frac{2\, A_2\, e^{\left(\frac{-E_{RDS}^a}{RT}\right)} P_{O_2}\, L_{Fe}^2\, B^2\ e^{\left(\frac{-2\,\Delta H_{ads\,NO}}{RT}\right)} P_{NO}^2}{\left(1+B\ e^{\left(\frac{-\,\Delta H_{ads\,NO}}{RT}\right)} P_{NO}\right)^2}$$

where A_2 and B stand for pre-exponential factors in the Arrhenius expression of the k_2 kinetic constant and the Van't Hoff expression of the $K_{ads\,NO}$ thermodynamic constant respectively.

In order to calculate the reaction rates obtained in the whole temperature range from both *operando* and gas phase data, estimated values for five independent parameters (A_2, B, L_{Fe}, E_{RDS} and $\Delta H_{ads\ NO}$) should first be estimated.

Preliminary processing of the gas phase data provided estimated values for E^a_{RDS} = 43 kJ.mol^{-1} and for NO adsorption heat $\Delta H_{ads\ NO}$ = -30 kJ.mol^{-1} (see section 3.3.3).

Estimate for 2 A_2 P_{O2} L_{Fe}^2 was obtained from the slope of the following plot:

plot 3 $$\left(\frac{\mathbf{1}}{\mathbf{slope\ (plot\ 2)_T}}\right)^{\mathbf{2}} = \mathbf{f}\left(\mathbf{e}^{\left(\frac{-\mathbf{E^a_{RDS}}}{\mathbf{RT}}\right)}\right)$$

Estimate for B was obtained from the slope of the following plot:

plot 4 $$\frac{\boldsymbol{slope\ (plot\ 2)_T}}{\boldsymbol{y-intercept(plot\ 2)_T}} = \boldsymbol{f}\left(\boldsymbol{e}^{\left(\frac{-\boldsymbol{\Delta H_{ads\ NO}}}{\boldsymbol{RT}}\right)}\right)$$

Estimate for L_{Fe}^2 was obtained from the slope of the following plot:

plot 5 $$\left(\frac{\mathbf{1}}{\mathbf{slope\ (plot\ 2)_T}}\right)^{\mathbf{2}} = \mathbf{f(slope\ (plot\ 1)_T)}$$

Table 5 reports the whole estimated values together with their optimized values obtained after minimization of SD for the reaction rate calculated using both eq. 8 and eq. 9.

Table 5. Optimization of the kinetic parameters when considering RDS (2.1)

	Estimated values	Optimized values
2 A_2 P_{O2} L_{Fe}^2	401	5.91 10^{+3}
E^a_{RDS} / kJ.mol^{-1}	43.0	52.4
B	0.383	1.32 10^{-3}
$\Delta H_{ads\ NO}$ / kJ.mol^{-1}	-30.0	-52.3
L_{Fe}^2	9.18 10^{-2}	9.80 10^{-2}
SD	2.68 10^{-4}	1.12 10^{-4}

3.3.5.2 Summary for whole data processing.

A similar methodology was applied for the eight remaining possible RDS (i.j). The number of parameters required to model the whole experimental data was always fixed to the minimum value (see first column of Table 6) and their initial estimated values were always in a reasonable range as indicated by the initial estimated standard deviation lying between 1.27 10^{-4} and 7.70 10^{-4}.

Table 6. Comparison of the SD values obtained after processing the whole data (various T and *operando* + gas) when considering the remaining possible RDS (i.j)

Hypothesis – number of necessary parameters	SD estimated values	SD optimized values
RDS (2.1) - 5	2.68 10^{-4}	1.12 10^{-4}
RDS (3.1) - 7	7.60 10^{-4}	6.59 10^{-5}
RDS (4.2) - 9	6.76 10^{-4}	6.65 10^{-5}
RDS (5.3) - 11	7.70 10^{-4}	6.87 10^{-5}
RDS (2.4) - 7	5.41 10^{-4}	6.78 10^{-5}
RDS (3.4) - 9	1.63 10^{-4}	7.02 10^{-5}
RDS (2.5) - 5	7.05 10^{-4}	6.56 10^{-5}
RDS (3.5) - 7	7.54 10^{-4}	6.36 10^{-5}
RDS (5.5) - 6	1.27 10^{-4}	1.07 10^{-4}

Analysing the SD optimized values reported in Table 6 in more details, it appears that RDS (2.1) at the intersection between plot 1 and plot 2 (Table 3) and RDS (5.5) at the intersection between plot SI 1 and plot SI 4 (Table 3) should be rejected in agreement with their corresponding high ΣSD values reported in Table 4. As a consequence, only RDS at the intercept between plot SI 3 and plot SI 4 (grey zone in Table 6) remain the most possible. The optimized SD values are however very closed the ones from the others (6.36 10^{-5} < SD < 7.02 10^{-5}) and a supplementary criterion will be welcome in order to identify the best hypothesis. Indeed, among the seven remaining hypothesis, four of them [(3.1), (4.2), (5.3) and (3.4)] involve the NO_2 desorption from iron as the RDS. Consequently, at a given temperature, the initial reaction rate should increase with the concentration of adsorbed NO_2 here noted as [*Fe_NO_2]. When processing the *operando* spectra reported at Fig. 3 the focus was put on the quantitative analysis of the mononitrosyl species band intensity that is proportional to their concentration

[*Fe_NO]. However, the spectra were also qualitatively described and even if band assignment was proposed as nitrate species for the 1620 cm^{-1} and adsorbed NO_2 for the 1612 one, it is worth noting that both bands may also characterize adsorbed NO_2 onto cationic site according to Hadjjivanov [20] and ref therein. Starting from this new assignment and considering hypothetical RDS (3.1), (4.2), (5.3) and (3.4), one should then observe an increase of the 1612 and 1620 cm^{-1} band intensity with the reaction rate. The semi quantitative analysis of Fig. 3 clearly shows that this is not the case. Indeed, Table 2 provides evidence that the reaction rate increases with [*Fe_NO] while Fig. 3 shows an opposite evolution between the 1878 cm^{-1} typical for [*Fe_NO] and the 1620-1612 cm^{-1} bands typical for [*Fe_NO_2].

As a conclusion, if any adsorbed *Fe_NO_2 are present on the FeFER800 catalyst under duty, their evolution does not match with their desorption being the RDS. Hypothetical RDS (3.1), (4.2), (5.3) and (3.4) should then be rejected.

Only three RDS then remain as good candidates: RDS (2.4), (2.5) and (3.5). Concerning RDS (2.4), as it involves Fe_O species that are not detected here by IR spectroscopy, we can not confirm or infirm this hypothesis. However, RDS (3.5) and RDS (2.4) require exactly the same number of parameters (7) for modelling the whole data. The SD value is thus calculated exactly the same way (similar denominator) and since the former RDS (3.5) leads to a slightly lower SD value than the later, the RDS (2.4) will further be rejected in the present work. Considering now RDS (2.5) and RDS (3.5), it is worth noting that the last one leads to the lowest optimized SD value. Moreover, RDS (2.5) and RDS (3.5) both relate to the same reaction mechanism whose RDS was previously described as the Fe_OONO dissociation into Fe_O and NO_2 [23]. This step exactly consists in our RDS (3.5) and our experimental data together with their original kinetic processing thus perfectly match with previous theoretical modelling. It is however important to specify that few modifications were made regarding the detailed mechanism proposed by Brüggemann et al [23] in order to fit with our *operando* data. More precisely, the Fe_OONO intermediate species was here noted as Fe_NOO_2 as a result from the interaction between the observed Fe_NO and O_2 from the gas phase. Finally, a good candidate for the IR band typical for this Fe_NOO_2

active intermediate species is the 1575 cm^{-1} one even if its low intensity and location at the tail of the broad 1620-1612 cm^{-1} doublet prevent from reliable quantitative analysis.

The best RDS was thus identified as the third step of mechanism 5. The values for the seven parameters required to calculate the corresponding reaction rate either form eq. SI 114 or eq. SI 117 are provided in Table 7.

eq. SI 114 $$r_m = k_3 K_{RNO} P_{O_2} [\ ^*Fe\_NO]$$

eq. SI 117 $$r_m = \frac{k_3 L_{Fe} K_{RNO} P_{O_2} K_{ads\ NO} P_{NO}}{1+(K_{RNO} P_{O_2}+1) K_{ads\ NO} P_{NO}}$$

Table 7. A summary of both initial parameters and optimized values obtained for the individual kinetic and thermodynamic parameters necessary to calculate the NO to NO_2 oxidation rate when considering RDS (3.5) as the best hypothesis.

Reaction rate parameters for RDS (3.5)	$K_3\ K_{RNO}\ PO_2$		$K_{RNO}\ PO_2$		$K_{ads\ NO}$		L_{Fe}
Parameters chosen for optimization	$A_3\ B_1\ PO_2$ / mmol.h^{-1}	E^a_{RDS} + ΔH_{RNO} / kJ.mol^{-1}	$B_1\ PO_2$	ΔH_{RNO} / kJ.mol^{-1}	B_2 / atm^{-1}	$\Delta H_{ads\ NO}$ / kJ.mol^{-1}	L_{Fe} / mg^{-1}
Estimated values	1.37 10^{+3}	44.0	3.70 10^{+2}	11.2	6.50	-20.0	0.3
Kinetic and thermodynamic individual parameters	$A_{3\ opt}$ / mmol.h^{-1}	E^a_{RDS} / kJ.mol^{-1}	B_1 / atm^{-1}	ΔH_{RNO} / kJ.mol^{-1}	B_2 / atm^{-1}	$\Delta H_{ads\ NO}$ / kJ.mol^{-1}	$L_{Fe\ opt}$ / mg^{-1}
Optimized values	9.23	33.7	2.03 10^{+3}	12.6	2.09 10^{-1}	-22.7	3.94

The top part of Table 7 summarizes the initial data set and the estimated values that were used as input before running the several iterations required to get the minimal SD value reported in Table 6. It seems important here to remind that the molar extinction coefficient for the mononitrosyl species Fe_NO was not determined and that the [Fe_NO] values used for the data modelling are the bare heights of the IR peak normalized per mg of powder (in

mg^{-1}) that are indeed proportional to molar specific concentrations. For dimensional concordance, the total specific iron concentration $L_{Fe\ opt}$ is thus also obtained in mg^{-1} and as a consequence the $A_{3\ opt}$ value is obtained in $mmol.h^{-1}$. The only right parameter is thus the $A_{3\ opt}\ L_{Fe\ opt}$ product whose value equals 3.64 10^{+1} $mol.h^{-1}.g^{-1}$. Given the nominal iron weight loading (0.90 wt%), it is then possible to estimate $L_{Fe\ real}$ = 1.61 10^{-4} $mol.g^{-1}$ and get a value for $A_{3\ real}$ = 2.26 10^{+5} h^{-1}.

Finally, the Fig. 8 provides the whole experimental data obtained in this work together with their best fit obtained using the optimized values reported in Table 7. Both the reaction rate as a function of surface mononitrosyl concentration (upper part) and the reaction rate as a function of P_{NO} (lower part) theoretical curves (in red) present a rather goof fit of the experimental points. The curve fitting quality obviously increases with the reaction temperature and one suggests that traces of water impurities may affect the reaction mechanism [23] specially in the low temperature range.

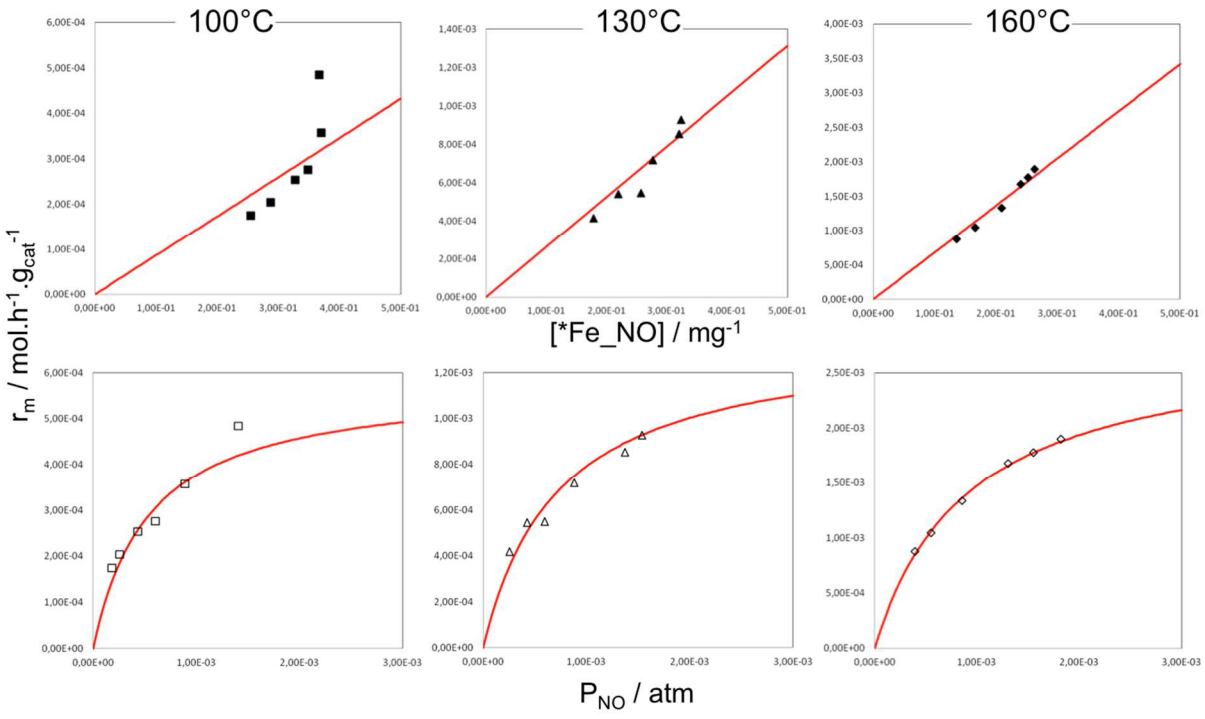

Figure 8. Best experimental data fit (in red) of the NO to NO_2 oxidation rate (RDS 3.5) obtained over FeFER800 as a function of [*Fe_NO] (Upper part) and P_{NO} (Lower part). The whole temperature data (Left) 100°C, middle (130°C) and right (160°C) were fitted with the optimized individual parameters reported in Table 7.

4. Conclusions

This work aimed at clarifying the NO to NO_2 reaction mechanism over iron based zeolites. Due to the recent trend to develop SCR catalysts directly wash-coated onto the DPF monolith, highly hydrothermal resistant materials are under current development. For this reason, iron ferrierite was here considered as an interesting stable zeolitic structure and its ageing under hydrothermal conditions at 800°C was achieved to yield the FeFER800 catalyst. The textural analysis evidenced that compared to the 'fresh' FeFER sample, FeFER800 presents both higher microporous and mesoporous volumes. This result is tentatively explained by an agglomerate dislocation phenomenon occurring under hydrothermal aging ('pine cone' opening) that would lead to a higher amount of isolated individual crystals. This phenomenon is 'by chance' in favor of a thorough kinetic study since the later requires working in the chemical regime for which internal and external mass transfer should not be limiting steps. The absence of external diffusion limitation with FeFER800 was checked with a dedicated experiment while internal diffusion limitation was assumed minimum from comparison with literature data.

After, these preliminary verifications, a detailed mechanistic study was undertaken through a kinetic approach involving both catalyst data (*operando*) and gas phase data. Five distinct hypothetical mechanisms were considered with each of their individual step being considered as possible rate determining ones. A set of more than one hundred equations was obtained and a first data processing consisting in a linearization of reaction rates provided six distinct plots when *operando* data were used (iron mononitrosyls [*Fe_NO] were considered as the Most Abundant Reaction Intermediate) and five distinct plots when gas phase data were used (P_{NO}). Some plots could easily be rejected due to a strong disagreement between experimental data and theoretical ones. On another hand, most of them could reasonably be further considered when looking at the determination coefficient R^2 as the only parameter. A next approach thus consisted in the direct calculation of reaction rate at a given temperature as a function of experimental variables and estimated values for constants (from preliminary linearization work) and their further optimization through minimization of the Standard Deviation (SD) using non-linear optimization methods. Some other plots leading to the higher SD values were then rejected. At this step of the study, nine among nineteen distinct RDS (i.j) still remained as good candidates. Aiming at identifying the best one, the final approach consisted, for each remaining possible RDS (i.j), in processing simultaneously both the whole data (*operando* + gas) and the whole temperatures. Taking into account the resulting SD values after optimization and making a further look at the *operando* data with a focus on the semi-quantitative evolution of possible adsorbed NO_2 species, finally allowed the best hypothetical reaction mechanism and its associated RDS to be identified. The best mechanism determined in the frame of this study thus involves isolated iron sites onto which NO and O_2 co-adsorb and the corresponding rate determining step consists in the dissociation of the so-formed Fe_NOO_2 intermediate species. Activation energy and reaction enthalpy values were then obtained. Both the mechanism, among five independent ones and its RDS perfectly match with a preliminary work based only on theoretical considerations [23]. To the best of our knowledge, this is the first time that such an experimental work

involving the complementary kinetic processing of both *operando* and gas phase data is reported in the context of automotive depollution. This approach involving *operando* data in the kinetic processing is however highly promising. It was indeed also successfully applied in the context of alkane monomolecular cracking [26, 27].

5. Acknowledgements

The financial support provided by UNICAEN is acknowledged.

FIGURE CAPTIONS

Figure 1. SEM pictures for the fresh FeFER (left) and aged FeFER800 right (upper part). Analogy with a pine cone opening to illustrate the surface roughness creation (bottom part).

Figure 2. Verification of the absence of diffusional limitation for the 'fresh' FeFER catalyst (W- mass of the catalyst and G- total flow).

Figure 3. Iron nitrosyls intensity as a function of NO gas concentration at 100°C over FeFER800.

Figure 4. Five distinct hypothetical mechanisms for NO to NO_2 oxidation and their sequence of elemental steps.

Figure 5. Kinetic processing of data obtained over FeFER800 in the frame of RDS (2.1) at distinct temperatures (Left) 100°C, middle (130°C) and right (160°C). Upper part: Plot 1 relative to *operando* adsorbed species. Lower part: Plot 2 relative to gas phase data.

Figure 6. A summary of the possible plots arising from the kinetic processing of ***operando*** data over FeFER800; Temperature: Upper row 100°C, middle row 130°C, lower row 160°C.

Figure 7. A summary of the possible plots arising from the kinetic processing of **gas** data over FeFER800; Temperature: Upper row 100°C, middle row 130°C, lower row 160°C.

Figure 8. Best experimental data fit (in red) of the NO to NO_2 oxidation rate (RDS 3.5) obtained over FeFER800 as a function of [*Fe_NO] (Upper part) and P_{NO} (Lower part). The whole temperature data (Left) 100°C, middle (130°C) and right (160°C) were fitted with the optimized individual parameters reported in Table 7.

6. References

[1] Nitrogen oxides (NOx) emission (APE 002), in: E.E. Agency, (Ed.), Assessment published Jan 2014, Retrieved July 2, 2018, from: https://http://www.eea.europa.eu/data-and-maps/indicators/eea-32-nitrogen-oxides-nox-emissions-1.

[2] K. Hirata, N. Masaki, M. Yano, F. Akagawa, K. Takada, J. Kusaka, T. Mori, Development of an improved urea-selective catalytic reduction-diesel particulate filter system for heavy-duty commercial vehicles, International Journal of Engine Research 10 (2009) 337-348.

[3] A. Dittler, The application of Diesel particle filters-from past to present and beyond, Top. Catal. 60 (2017) 342-347.

[4] J.A. Sullivan, O. Keane, The role of Brønsted acidity in poisoning the SCR-urea reaction over FeZSM-5 catalysts, Appl. Catal., B 61 (2005) 244-252.

[5] J.-H. Park, H.J. Park, J.H. Baik, I.-S. Nam, C.-H. Shin, J.-H. Lee, B.K. Cho, S.H. Oh, Hydrothermal stability of CuZSM5 catalyst in reducing NO by NH_3 for the urea selective catalytic reduction process, J. Catal. 240 (2006) 47-57.

[6] A. Grossale, I. Nova, E. Tronconi, D. Chatterjee, M. Weibel, NH_3-NO/NO_2 SCR for Diesel exhausts aftertreatment: reactivity, mechanism and kinetic modelling of commercial Fe- and Cu-promoted zeolite Catalysts, Top. Catal. 52 (2009) 1837-1841.

[7] T.C. Watling, M.R. Ravenscroft, G. Avery, Development, validation and application of a model for an SCR catalyst coated diesel particulate filter, Catal. Today 188 (2012) 32-41.

[8] W. Kang, B. Choi, S. Jung, S. Park, PM and NOx reduction characteristics of LNT/DPF plus SCR/DPF hybrid system, Energy 143 (2018) 439-447.

[9] S. Andonova, S. Tamm, C. Montreuil, C. Lambert, L. Olsson, The effect of iron loading and hydrothermal aging on one-pot synthesized Fe/SAPO-34 for ammonia SCR, Appl. Catal., B 180 (2016) 775-787.

[10] S. Thomas, O. Marie, P. Bazin, L. Lietti, C.G. Visconti, M. Corbetta, F. Manenti, M. Daturi, Modelling a reactor cell for operando IR studies: From qualitative to fully quantitative kinetic investigations, Catal. Today 283 (2017) 176-184.

[11] S.B. Rasmussen, S. Perez-Ferreras, M.A. Bañares, P. Bazin, M. Daturi, Does pelletizing catalysts influence the efficiency number of activity measurements? Spectrochemical engineering considerations for an accurate operando study, ACS Catalysis 3 (2013) 86-94.

[12] R.W. Tschernich, Zeolites of the world, Geoscience Press, Inc. ed., Phoenix, Arizona, 1992.

[13] M.A. Vannice, Kinetics of catalytic reactions, Springer, New-York, 2005.

[14] F. Gao, E.D. Walter, E.M. Karp, J.Y. Luo, R.G. Tonkyn, J.H. Kwak, J. Szanyi, C.H.F. Peden, Structure-activity relationships in NH_3-SCR over Cu-SSZ-13 as probed by reaction kinetics and EPR studies, J. Catal. 300 (2013) 20-29.

[15] E. Ivanova, M. Mihaylov, K. Hadjiivanov, V. Blasin-Aubé, O. Marie, A. Plesniar, M. Daturi, Evidencing three distinct Fe^{II} sites in Fe-FER zeolites by using CO and NO as complementary IR probes, Appl. Catal. B 93 (2010) 325-338.

[16] V. Blasin-Aube, O. Marie, J. Saussey, A. Plesniar, M. Daturi, N. Nguyen, C. Hamon, M. Mihaylov, E. Ivanova, K. Hadjiivanov, Iron nitrosyl species in Fe-FER: a complementary Mossbauer and FTIR spectroscopy study, J. Phys. Chem. C 113 (2009) 8387-8393.

[17] J. Szanyi, J.H. Kwak, R.J. Chimentao, C.H.F. Peden, Effect of H_2O on the adsorption of NO_2 on gamma-Al_2O_3: an in situ FTIR/MS study, J. Phys. Chem. C 111 (2007) 2661-2669.

[18] G.M. Underwood, T.M. Miller, V.H. Grassian, Transmission FT-IR and Knudsen cell study of the heterogeneous reactivity of gaseous nitrogen dioxide on mineral oxide particles, J. Phys. Chem. A 103 (1999) 6184-6190.

[19] E.J.M. Hensen, Q. Zhu, R.A. van Santen, Extraframework Fe–Al–O species occluded in MFI zeolite as the active species in the oxidation of benzene to phenol with nitrous oxide, J. Cat. 220 (2003) 260-264.

[20] K. Hadjiivanov, Identification of Neutral and Charged NxOy Surface Species by IR Spectroscopy, Catal. Rev. - Sci. Eng. 42 (2000) 71.

[21] D.D. Eley, E.K. Rideal, Proc. Royal Soc. London A 178 (1941) 429.

[22] B.M. Weiss, E. Iglesia, Mechanism and site requirements for NO oxidation on Pd catalysts, J. Catal. 272 (2010) 74-81.

[23] T.C. Brüggemann, F.J. Keil, Theoretical investigation of the mechanism of the oxidation of nitrogen oxide on iron-form zeolites in the presence of water, J. Phys. Chem. C 115 (2011) 2114-2133.

[24] R. Brosius, D. Habermacher, J.A. Martens, L. Vradman, M. Herskowitz, L. Capek, Z. Sobalik, J. Dedecek, B. Wichterlova, V. Tokarova, O. Gonsiorova, NO oxidation kinetics on iron zeolites: influence of framework type and iron speciation, 6th International Congress on Catalysis and

Automotive Pollution Control (CAPoC6), Kluwer Academic/Plenum Publ, Brussels, BELGIUM, 2003, pp. 333-339.
[25] L. Capek, L. Vradman, P. Sazama, M. Herskowitz, B. Wichterlova, R. Zukerman, R. Brosius, J.A. Martens, Kinetic experiments and modeling of NO oxidation and SCR of NOx with decane over Cu- and Fe-MFI catalysts, Appl. Catal., B 70 (2007) 53-57.
[26] S.A. Kadam, H. Li, R.F. Wormsbecher, A. Travert, Impact of zeolite structure on entropic–enthalpic contributions to alkane monomolecular cracking: an IR operando study, Chemistry – A European Journal 24 (2018) 5489-5492.
[27] H. Li, S.A. Kadam, A. Vimont, R.F. Wormsbecher, A. Travert, Monomolecular cracking rates of light alkanes over zeolites determined by IR operando spectroscopy, ACS Catalysis 6 (2016) 4536-4548.

GRAPHICAL ABSTRACT

NO to NO_2 mechanism over FeFER through an *operando* kinetic study

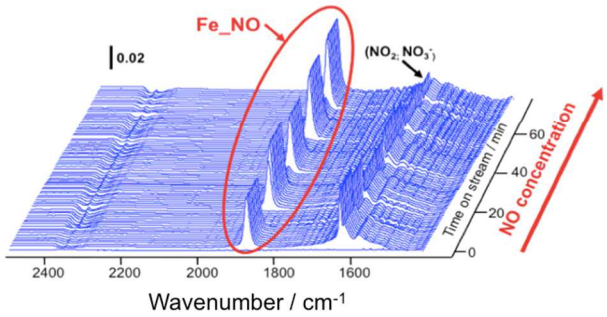

$Fe + NO \leftrightarrows Fe\_NO$

$Fe\_NO + O_2 \leftrightarrows Fe\_NOO_2$

$Fe\_NOO_2 \rightarrow Fe\_O + NO_2$

$Fe\_O + NO \leftrightarrows Fe\_NO_2$

$Fe\_NO_2 \leftrightarrows NO_2 + Fe$

$2NO + O_2 = 2NO_2$